Korean J. Chem. Eng., 39(3), 785-797 (2022)
DOI: 10.1007/s11814-021-0929-7

pISSN: 0256-1115
eISSN: 1975-7220

Insight into mechanical, thermal, and chemical stability of polysulfone-based membranes for the separation of O_2/N_2

Suchhanda Srabanee Swain†, Lakshmi Unnikrishnan, Smita Mohanty, and Sanjay Kumar Nayak

School for Advanced Research in Polymers (SARP), Laboratory for Advanced Research in Polymeric Materials (LARPM),
Central Institute of Plastics Engineering & Technology (CIPET), B/25, CNI Complex,
Patia, Bhubaneswar - 751024, Odisha, India
(*Received 18 March 2021 • Revised 27 July 2021 • Accepted 15 August 2021*)

Abstract−MMMs have opened up a new window in gas separation and purification applications, but the actual viability can be reckoned on the basis of performance achieved in realistic feed conditions. This research highlights the selection of silica-decorated graphene for the first time to prepare nanocomposite membranes. XRD, Raman, and UV validated the existence of different fillers within the host Polysulfone (PSf), while TEM authenticated their distribution. The burst strength and thermal properties were also investigated for the prepared samples. This study also covered a prudent step towards resolving the dominant ingredients, which routinely appraise the stability and durability of the membranes. These indexes are long-term gas permeation stability up to 120 hours coupled with sustainability against hydrothermal and chemical resistance under various conditions similar to real-life gas separation applications. Finally, the report demonstrates that the nanohybrid integrated membrane systems display optimum performance and stability in all the aspects as compared to their parent counterparts: PSf/mSiO_2 and PSf/GO.

Keywords: Silica Decorated Graphene, High Performance MMMs, Better Burst Strength & Thermal Stability, Long-term Permeation, Hydrothermal and Chemical Resistance

INTRODUCTION

Researchers have recently focused their attention on the development of a high performance membrane system, which must be contemplated as a viable candidate for diverse lab as well as large-scale industrial gas separation and purification applications. The eye-catching momentums as received from numerous reports have endowed the membrane technology as an affordable and competent approach for the separation of various gases [1]. The introduction of mixed matrix membrane (MMM) has rapidly experienced substantial growth, breakthrough, and enormous prosperity for the selective permeation of penetrant with greater perm-selectivity [2]. Numerous legitimate attempts have been devoted to identifying unique membrane-forming materials, which would retain promising characteristics to realize excellent performance. Besides, the separation behavior should surpass the "Robeson upper bound limit". It is an empirical limit that has been envisaged as the benchmark against which the viability of distinctive membranes is compared [3]. Nevertheless, frequent emergence of a few prominent issues, including interfacial adhesion between two phases, selection of appropriate filler on the basis of size, pore diameter, attachment of different functionalities, affinity to the chosen gases, and degree of dispersion or distribution status within the matrix must be encountered to accomplish the desired properties for the developed MMMs [4].

These consistently arising issues need to be suitably addressed in order to attain the expected performance. In the middle of recognition of phenomenal dispersed phase, NPs (silica -SiO_2) decorated graphene has been greatly recommended, inspired from its advantageous features [5]. This nanohybrid has been successfully implemented in miscellaneous areas, such as bio-medical application [6], liquid purification [7], anti-corrosion hydrophobic coating [8], Li-ion batteries [9], and biosensors [10]. To the best of our knowledge, there is no report claiming the development of nanocomposite membrane structure with the incorporation of this particular hybridized nanosheet for the separation and purification of gases. This nanohybrid has been encompassed with multi-functionalities, which would play an imperative role to intensify the dispersive characteristics, ultimately reinforce the interfacial interaction between the phases [11]. Further, it not only boosts an affinity with the molecular species but also contributes to facilitating the origination of several diffusion channels or pathways at the interfacial region within the developed membrane. As a consequence, this stimulates the origination of smooth transport avenues for the resistance-free permeation of gases through the hybrid system.

The proficiency of the membrane is consistently predicted on the basis of the performance achieved on bench-scale under favorable absolute conditions and setups. But a conspicuous deviation may be realized with its implementation under realistic processing parameters for large-scale industrial purposes [2]. Thus, it is extremely difficult to translate the performance of the system from small-scale lab setting to the conditions of real-life separation application. Durability and long-term stability are the crucial factors to evaluate the authenticity of the performance. Also, hydrothermal stabil-

†To whom correspondence should be addressed.
E-mail: suchhandaswain@gmail.com

ity is a predominant parameter to appraise the extent of capability of a membrane towards the water vapor environment. The manifold impurities, such as SO_2, NO_2, mostly persist within the supplied gas stream; those may combine with the absorbed moisture on the surface of the membrane and possibly form acid. Consequently, it would degrade the structure and decline the performance of the system [12].

This investigation highlights the development of high performance MMMs with the selection of surface-decorated silica based graphene nanohybrid as the potential dispersed phase along with its parent counterparts. Especially, it concentrates on inquiring viability of the prepared membranes, in terms of mechanical and thermal behavior. Further, the long-term permeation stability, hydrothermal, and chemical resistance have been assessed for the prepared samples in accordance with the transport rate of targeted gaseous species. Also, the deviation has been analyzed from the originally recorded permeability and selectivity of the individual samples at the regular parameters under the prescribed applied conditions.

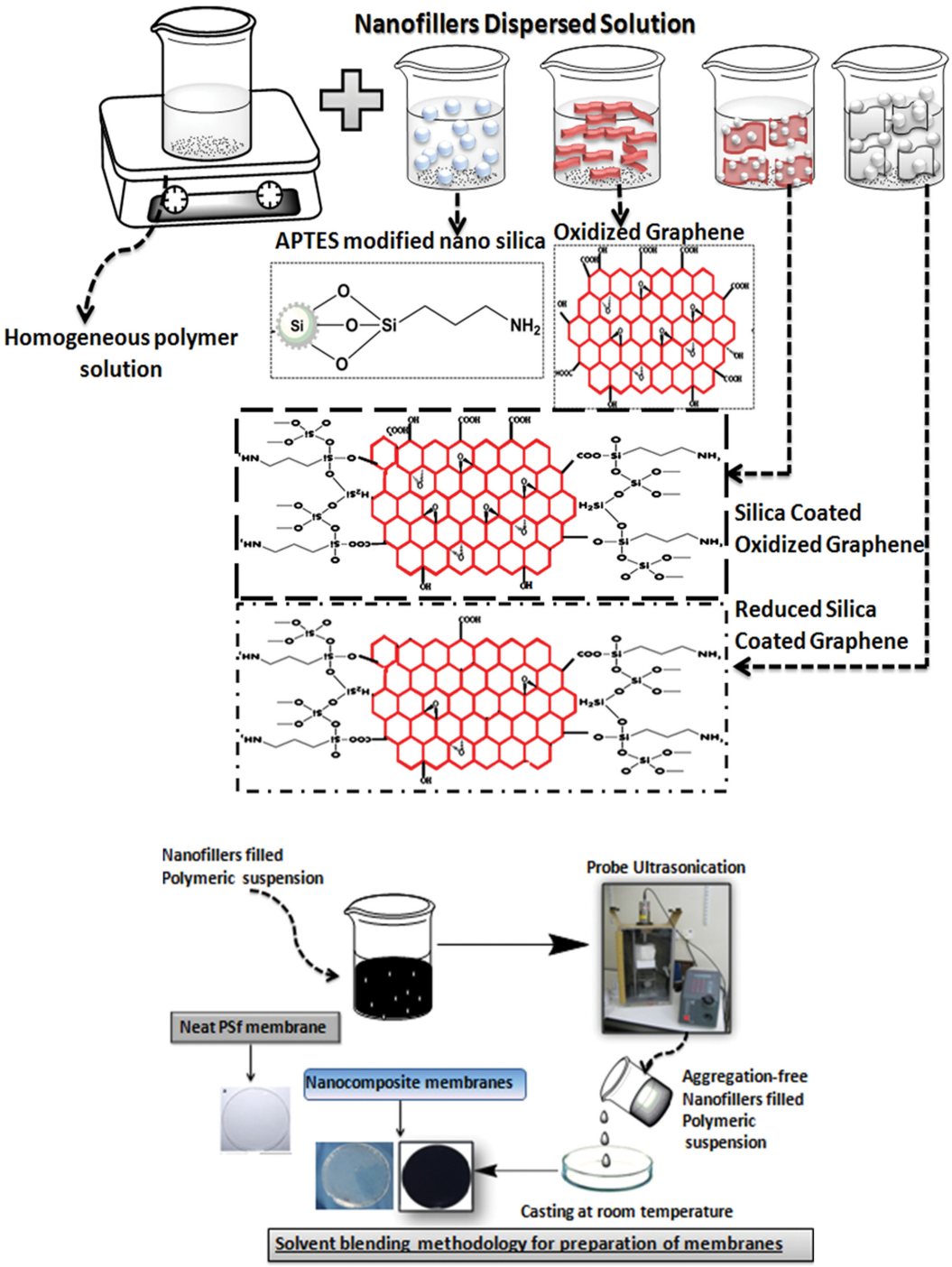

Fig. 1. Preparation process of nanocomposite membranes.

MATERIALS AND EXPERIMENTAL METHODS

1. Materials

Graphite powder (20 μm) was supplied by Aldrich. GO was prepared by modified Hummer's method and the required chemicals: $NaNO_3$, $KMnO_4$ were procured from Merck, H_2SO_4, HCl were purchased from HiMedia, and H_2O_2 aqueous solution was provided by RFCL Gelest. The surface decoration of GO was conducted through silica self-assembly precursor solution by *in-situ* sol-gel technique. The precursor solution consisting of NH_4Cl with M.W 53.49 g/mol and TEOS ($C_8H_{20}O_4Si$) (M.W 208.33 g/mol) was gained from Aldrich, APTES of M.W 221.37 g/mol, Ethanol (C_2H_6O) with M.W 46.068 g/mol were supplied from HiMedia, and NaOH of M.W 39.99 g/mol was acquired from Fisher. The prepared nanohybrid was reduced by non-toxic L-Ascorbic acid ($C_6H_8O_6$) with M.W 176.13 g/mol was acquired from Fisher. Tetrahydrofuran (C_4H_8O) of M.W 72.11 g/mol with purity of ~99.00% was provided by HiMedia. Polysulfone (PSf) pellet (M.W 35,000) and nano silica (SiO_2) with specific surface area (SSA) between 175 to 225 m^2/g as measured by BET were supplied by Aldrich.

2. Procedure to Develop Membranes

The detailed methodology for the synthesis and relevant characterization studies of APTES modified nano silica ($mSiO_2$), graphene oxide (GO), silica decorated oxidized graphene (SGO), and silica decorated reduced graphene (RSGO) have been discussed in our previous research [13]. The unfilled Polysulfone (PSf) membrane and different fillers comprising MMMs were prepared through solution blending technique. Fig. 1 illustrates the systematic scheme to prepare the membranes. The method for the preparation of different membranes was described in our earlier report [14]. In this investigation, 04 numbers of nanofillers ($mSiO_2$, GO, SGO, and RSGO) incorporated membrane systems were fabricated and designated as C_1, C_2, C_3, and C_4, respectively, in the next section, while the nascent PSf membrane was entitled as N_0.

3. Characterization

3-1. X-RD Analysis

The structural behavior1 of the samples was determined by X-ray diffractometer (Shimadzu XRD-7000L, Japan) employing CuK_α radiation (λ=1.514 Å). The samples were examined at a scanning rate of 2°/min over a range of diffraction angles with 2θ interval from 3-70°.

3-2. Raman Spectroscopy

The Raman spectra of the membrane systems were analyzed by micro Raman spectrometer (M820, Renishaw, UK). It was conducted at room temperature with an excitation wavelength of 532 nm and laser power of 0.5%. The spectra were measured at 10 s exposure time within the range from 101.77 to 3502.19 Raman shift/cm^{-1}.

3-3. Ultraviolet-visible (UV) Spectroscopy

The UV spectrum of the membranes was recorded by UV-Shimadzu 2450. The spectra were analyzed within the wavelength (λ) range from 200 to 800 nm.

3-4. Transmission Electron Microscopy (TEM)

The dispersion quality of the nanofiller phase throughout the host PSf matrix was examined by TEM JEOL-JEM1400, Japan at an accelerating voltage of 120 kV. The samples were cut by Leica ultracut microtome equipped with a diamond knife. The ultrathin section of the sample was placed on the copper grid for imaging.

3-5. Burst Strength

The burst strength of the prepared samples was measured by burst strength tester BST-A101 within a pressure range from 0.1 to 14.0 kgf/cm^2.

3-6. Thermal Properties (TGA, DSC)

The thermal stability of the membranes was studied by thermogravimetric analyzer (TGA, Q50, TA Instruments USA). The samples of around 7-10 mg were scanned at a linear heating rate of 10 °C/min over the temperature range from 30 to 800 °C.

Differential scanning calorimetry (DSC) analysis was conducted (Q20, M/s TA Instruments, USA) to measure glass transition temperature (T_g) of the membranes. The samples of about ≤7 mg were scanned from room temperature to 350 °C with a heating rate of 10 °C/min under a nitrogen atmosphere.

4. Gas Permeability Coefficients

Gas transmission rate (GTR) (N530, GBPI, Packaging equipment, Hemtech) was utilized to analyze the transmission rate of penetrants through the membrane systems. We selected the light gases (O_2 and N_2) in this work, which exhibit the kinetic diameters of 3.46 and 3.64 Å, respectively. The measuring range was fixed at [m^3(STP) m^{-2} h^{-1} bar^{-1}] within a temperature from 20 to 30 °C and the permeation rate of single gas was conducted separately as per ASTM D 1434 at 1 bar constant feed pressure. The area and thickness of the exposed membrane samples are within the range of 50 cm^2 and 75 μm, respectively. The permeability coefficients (P_i and P_j) of the gases were analyzed by taking three replicate samples from each system and the average values have been mentioned. Subsequently, the ideal selectivity factor ($\alpha_{i/j}$) can be estimated by using the equation as follows, which can be stated as the ratio of the pure gas permeances (P_i) over (P_j):

$$\alpha_{i/j}=\frac{P_i}{P_j}$$

5. Long-term Permeation, Hydrothermal Stability, and Chemical Resistance of the Systems

The long-term stability was evaluated by exposing the samples for continuous gas permeation testing up to 120 hours without any interruption at the similar testing procedure as previously mentioned. Permeabilities were listed at each 24 hours of the testing time for the sample. To determine the hydrothermal stability, the neat PSf and nanocomposites were located over a concealed container occupied by distilled water and allowed to heat at 100 °C for 12 hours to maintain a factitious vapor environment under lab-scale conditions. After the specified time period, the samples were detached and conserved for parched at 60 °C for 12 hours prior to the gas permeation testing. A similar procedure was conducted for evaluating the chemical resistance of the samples, instead, an acidic and alkaline medium with pH of 1 and 14 were perfectly maintained, respectively. The samples were placed separately under diluted sulfuric acid and ammonia solution. The treated samples were dried prior to testing.

RESULTS AND DISCUSSION

1. XRD (X-Ray Diffractometer)

Fig. 2 depicts the XRD plots of the samples (a) PSf (N_0) (b) PSf/

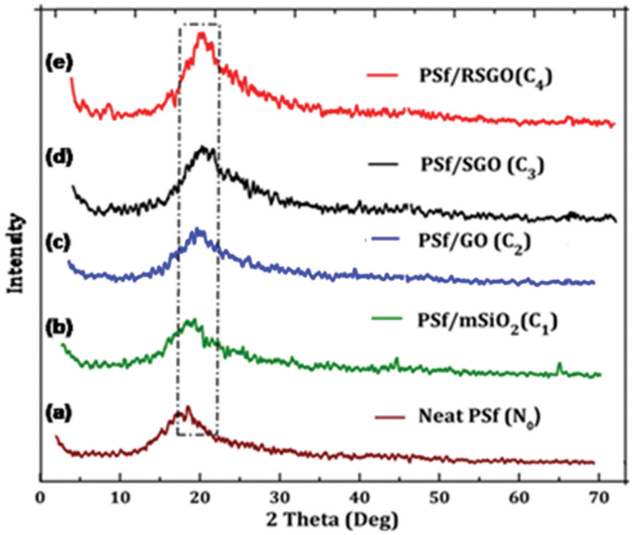

Fig. 2. XRD plot of membrane systems (a) Neat PSf (N_0), (b) PSf/$mSiO_2$ (C_1), (c) PSf/GO (C_2), (d) PSf/SGO (C_3) and (e) PSf/RSGO (C_4).

$mSiO_2$ (C_1) (c) PSf/GO (C_2) (d) PSf/SGO (C_3) and (e) PSf/RSGO (C_4). N_0 displayed a broad peak at 20° with *d*-spacing of 4.74 Å, indicating amorphous structural characteristics [16]. However, the bands of MMMs were slightly shifted to a lower angle with conspicuous decrement in the broadening of peaks, which signified the interaction between the PSf chain and incorporated fillers [15]. The *d-spacing* was also recorded higher, confirming the perceptible change in the structure after consequent insertion of the filler phase. However, the basic framework of the native N_0 membrane was discerned in all the nanocomposites.

For C_1 sample, the band was observed at 2θ=17° with *d-spacing* of 5.12 Å. It accredited the incorporation of the silica segments into the nascent PSf matrix. This diffractogram implies a fragile influence on the crystallization behavior owing to the entrenched interaction between silanol groups with the existing sulfone in PSf backbone. The chain packing was revised by means of hydrogen bonding that possibly entangled the PSf within silica network. Rafiq et al. [17] investigated an analogous trend for the SiO_2 embedded nanocomposite.

The characteristic peak of GO was almost weakened as pictured in the XRD diagram of C_2, suggesting an exfoliated morphology with depreciated van der Waal's forces. The diffraction angle at 18° with a greater *d*-spacing of 4.56 Å was recorded, which indicated intercalation of the PSf chain segments into the nanosheets. The expanded spacing might be elucidated to the attachment of the polar groups in terms of hydroxyl, epoxy at the basal plane and carbonyl, carboxyl groups at the edges along with the presence of a number of water molecules, which absorbed within the graphitic gallery [18] as reported by Ionita et al. for GO based system.

C_3 hybrid system exhibited a broadened peak, implying exquisite intercalation of hybridized nanosheets into the PSf segments. The increment in the diffraction band to nearly 3° than the counterparts (C_1 and C_2) and a slight enlarged *d-spacing* of 5.93 Å persuaded the presence of multi-functionality. The decoration of silane moieties precluded the restacking propensity of the sheets and agglomeration tendency of the particles. Besides, a supplementary synergistic effect might have been established, which reinforced the role of the hybrid dispersed phase within the PSf [19]. The interaction of SGO led to the creation of intermolecular periodicity and regular packing. Harei et al. reported a similar trend for SiO_2-GO filled epoxy nanocomposites [20].

A closer *d-spacing* of 3.85 Å and broadness in reflection was observed for C_4 hybrid system. It suggested conjugated π-π networks (sp^2 carbon) had restored with the removal of hydroxyl and epoxy groups from the basal plane. The appearance of the amorphous peak substantiated the grafting of silane moieties on the surface of graphene and attached to the PSf backbone.

2. Raman Spectroscopy

The received Raman spectra of the membranes are displayed in Fig. 3. The Raman spectrum of the native N_0 consisted of the peaks at 1,142 and 1,584 cm^{-1} corresponds to asymmetric C-O-C and aromatic ring chain vibration, respectively, as presented in (a). The peak at 788 cm^{-1} might be correlated to the asymmetric C-S-C bonding as discussed by Ionita et al. [16].

The spectrum of C_2 as shown in (b) illustrates the obvious appearance of a number of humps, demonstrating the intrinsic amorphous halo structural characteristics. The existence of a few bands at higher wavenumbers suggested the presence of Si-OH, isolated silanol groups, and the interacted silanol-sulfone bonding [21]. Si-O-Si siloxane bond is centered at 1,154 cm^{-1} indicating the attachment of organosilane molecule. The Raman intensity of the nano silica is weak; hence it is difficult to differentiate all the observed signals. However, the documented outcome has conveniently implied the incorporation of $mSiO_2$ into the PSf backbone [22].

The spectrum in Fig. 3(c) is dominated by the presence of two prominent bands D and G at 1,342 and 1,596 cm^{-1}, respectively, along with the 2D band at 2,932 cm^{-1}. The D band denotes to sp^3 disordered carbon structure associated with vacancies at edges and grain boundaries referred to as out-of-plane breathing mode of A_{1g} translational symmetry. G band is termed as the planar configuration of sp^2 ordered crystalline stacking of graphite-like structure and the stretching movements to in-plane E_{2g} phonon mode [5]. It can be noticed that the intensity of the D band was predominantly heightened owing to the defective structure and deformation, which is ascribed to the dense existence of exfoliated sheets containing oxygen-rich groups [16]. The G band might be overlapped by the peak of aromatic rings of the chain segments implying the favorable insertion of the GO into the neat PSf membrane as described by Lee et al. [23].

The spectrum of hybrid C_3 system displayed the shifting of the characteristic peaks of GO to higher wavenumbers at 1,350 and 1,602 cm^{-1} corresponding to the D and G bands, respectively, as shown in Fig. 3(d). The shifting of these bands revealed exfoliation and better interfacial interaction of the hybridized sheets within the matrix. Further, the existence of few peaks at lower wavenumbers (792 and 1,146 cm^{-1}) claimed the obvious attachment of the hydrated silicate network on the surface [20]. The band intensity ratio (I_D/I_G) was found to be 0.99 for the hybrid membrane, while the GO impregnated PSf system exhibited a lower value of 0.80. This outcome insisted on the formation of disordered structure owing

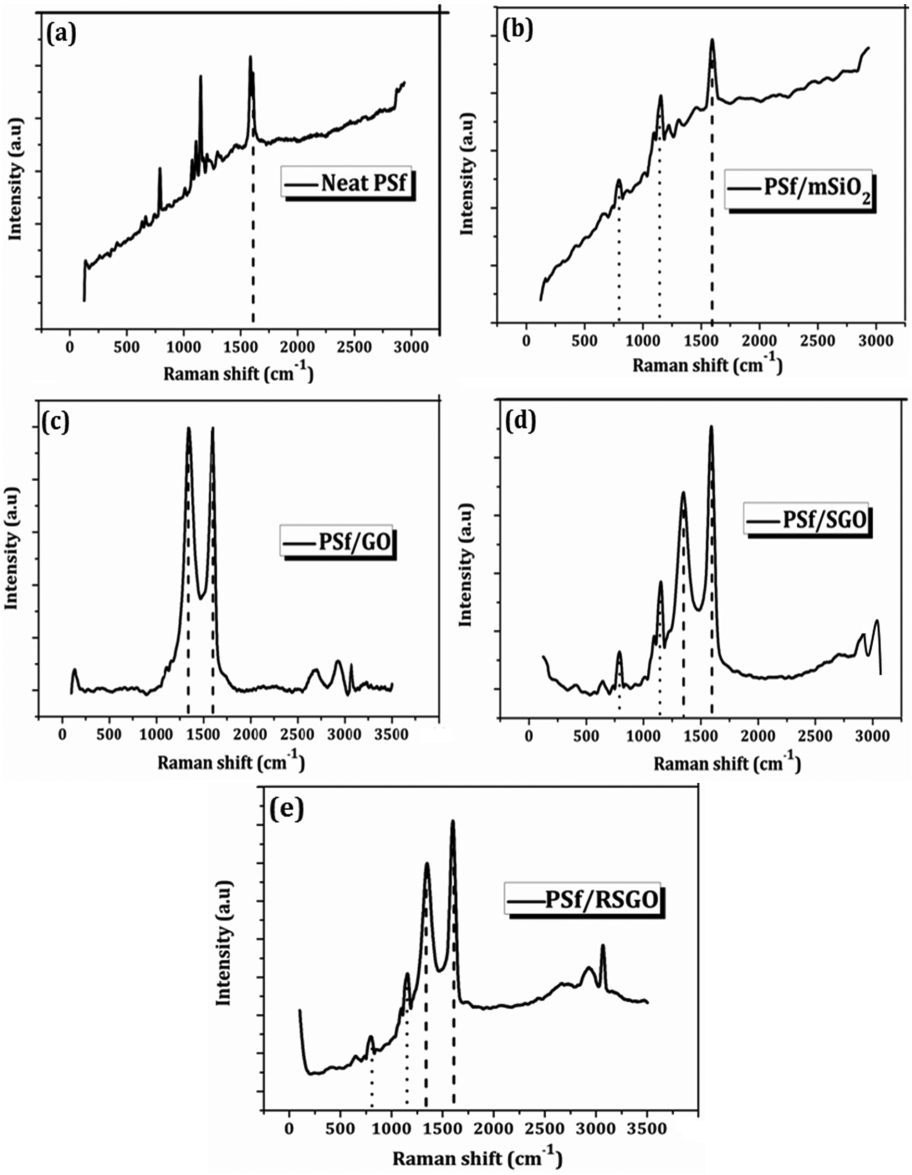

Fig. 3. Raman spectra of membrane systems: (a) (N_0), (b) (C_1), (c) (C_2), (d) (C_3), (e) (C_4).

to the attachment of multifunctional groups within the hybrid system. Apart from this, the peak related to asymmetric C-S-C bonding and aromatic ring vibration can be supposedly identified. The observation of these bands validated the addition of SGO into the host PSf matrix.

The D and G bands, as represented in (e) for the C_4 nanocomposite, was indexed at 1,359 and 1,609 cm^{-1}, respectively. The 2D band was found broadened, illustrating the arrangement of new graphitic in-plane sp^2 domains with shortened cluster size by virtue of the stretching of C-C bonding and scattering of phonon mode [24]. A higher I_D/I_G ratio of 1.4 was figured for the reduced hybrid system than the SGO integrated sample. Moreover, the existence of the bands related to the silicate network and PSf, as explained earlier, was identified in the spectrum.

3. Ultra-Visible (UV) Spectroscopy

UV spectra of the membranes are depicted in Fig. 4. The absorbance at 280 nm was recorded for N_0 corresponding to π-π* electron orbital transition of aromatic benzene rings [25].

C_1 membrane displayed an absorbance with λ_{max} of 265 nm, validating the existence of silanol groups. The absorbance at 350 nm shall be ascribed to the attachment of organosilane on the silica networks. Moreover, the defected structure might have originated owing to the oxygen vacancies and the presence of silica segments on the surface of C_1 [8]. In C_2 nanocomposite, the π-π* transition of aromatic C=C bonds associated to hexagonally arrayed sp^2 structure was shifted to 201 nm. This might be attributed to the interaction of GO within PSf matrix. Meanwhile, the n-π* transition related to C=O bonding was not significantly altered, which was noticed at 292 nm and confirmed the dense attachment of oxygen-rich groups [16].

The presence of a narrow peak at 203 nm was recorded for the C_3 system. The peak at 254 nm was accompanied by a small peak

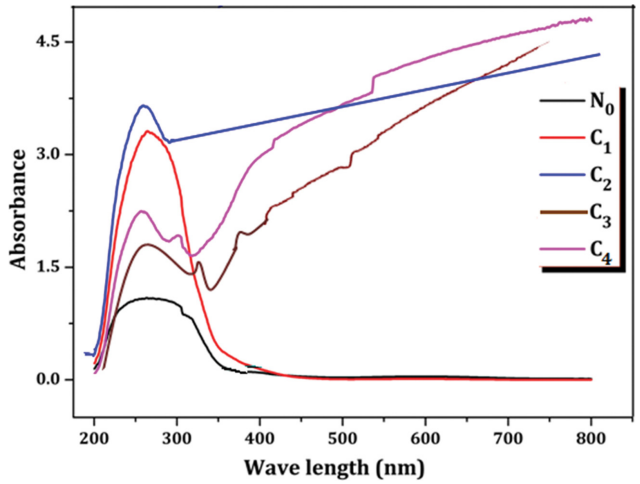

Fig. 4. UV spectra of membrane samples.

at 320 nm, which might have originated as a result of the excitation of plasmon graphitic. The red-shifting was attributed to the loss of stacking layers, indicating the formation of disordered structure within the membrane. This suggested strong interaction between the nanosheets attached silane moieties with PSf matrix [11]. The broadness in the peak confirmed oxygen vacancies and defected center owing to the change in surface chemistry with the attachment of multifunctionalities in the hybrid membrane. The bands related to silane moieties and oxygen active groups in C_3 insisted on proper distribution of the nanohybrids within PSf. From the spectrum of C_4, red shifting of the plasmon peak to 260 nm provided strong evidence for the insertion of RSGO into the PSf with the formation of aromatic C=C bonding. The broad shoulder peak vanished, demonstrating the increment of π-electron concentration and restoration of conjugated sp^2 carbon after the reduction.

4. Transmission Electron Microscopy (TEM)

TEM was carried out to investigate the distribution and disper-

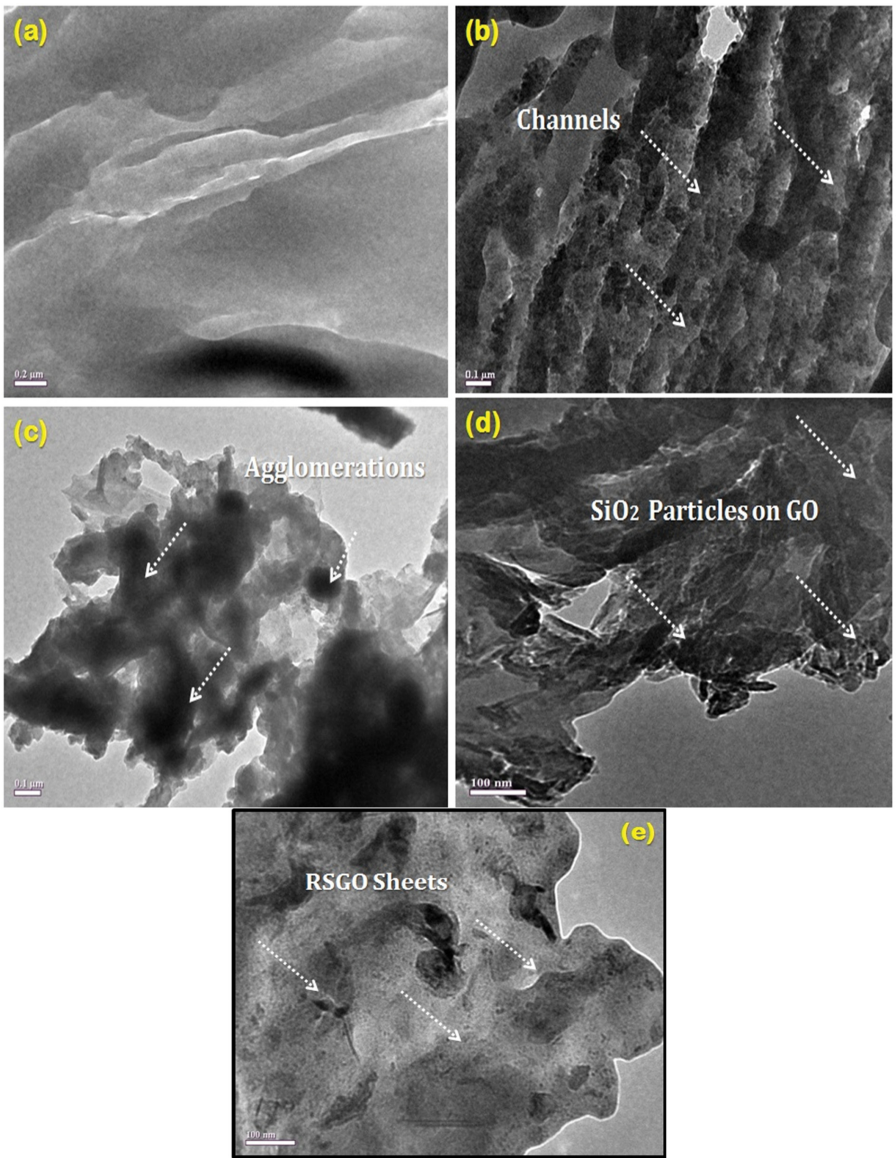

Fig. 5. TEM micrographs of membrane samples: (a) N_0, (b) C_1, (c) C_2, (d) C_3 and (e) C_4.

sion status of divergent fillers throughout the host matrix. Fig. 5 represents the TEM micrographs of the unfilled PSf and its nanocomposites. A clear, smooth surface with defect-free structural feature was demonstrated for the N_0 as displayed in (a). The appearance of some superfluous gaps and open spaces indicated rapid gelation of low viscose polymeric solution [8].

Image (b) displays an uneven dispersion pattern of $mSiO_2$ within PSf, which could be perceived due to the position of undesired agglomerates and clusters on the surface. It seemed like the particles were extracted from the surface and the gaps originating between the phases illustrated poor interfacial interaction. Further, the inorganic domains are not distributed like the isolated particles but fused together forming a chain-like architecture and heterogeneous morphology. The interfacial voids originated by virtue of particle clusters and massive structural defects, which appear as bright contrast in the micrograph [27]. This category of morphological view is proclaimed as "sieve in a cage", as reported by Adachi et al. [21]. The particle agglomeration within C_1 may also constrain the gas transportation path.

The micrographs of the nanocomposites comprising GO or GO-derived hybrids depicted ultrathin structures with folded and wrinkled features as well as silk-like morphology. Fig. 5(c) shows a translucent and disordered rippled structure with the appearance of superfluous gaps or crevices indicating the presence of GO. Also, it suggests the demolition of van der Waal interactions between the layers with the introduction of oxidative functionality [16]. The appearance of black dot-like structure or the specific dark portion might have affirmed the flocculation and restacking pattern of the sheets within the PSf. Further, the characteristic features of GO also created a long and tortuous avenue for the permeation of gases [18].

The image as depicted in (d) disclosed the appearance of creases and roughened texture with better exfoliation of the hybridized nanosheets throughout the host PSf without any obvious segregation. No visible cracks could be identified from the surface, suggesting that the hybrid system might not suffer embrittlement [19]. It exhibited improved dispersive characteristics by the dense grafting and precipitation of silane moieties on the corrugated sheets. Especially, uniform, homogeneous adsorption of SiO_2 on the basal plane contributed to the enhancement of interfacial morphology for the hybrid system. Moreover, the synergistic effect might have assembled between the membrane-forming materials, which could prevent the aggregation and re-stacking propensity of individuals [11]. The formulated nanochannels might have led to irregular protuberances. These configurations are favorable to provide better surface area, which would facilitate smooth permeation of gases through the hybrid system [20].

From image (e), long sharp lines with rougher morphology are observed. The presence of corrugation, folded flake, and scrolling delineates the characteristic geometries of intrinsic graphene. The existence of a number of holes and voided structures can be identified, which might be ascribed to the evacuation of oxygen functionalities and residual water molecules from the graphitic gallery. Further, the existence of high-density, close-packed SiO_2 grains on the surface of graphene confirms successful insertion of RSGO into the PSf matrix [9].

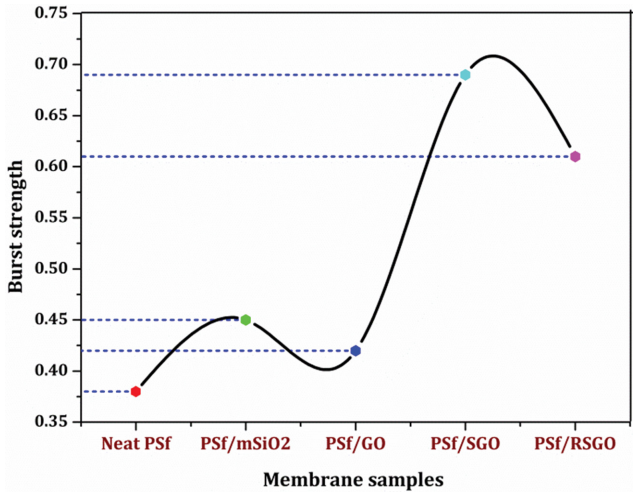

Fig. 6. Burst strength of membrane samples.

5. Burst Strength

Burst pressure can be represented as a realistic reflection of strength to measure the extent of force needed to rupture the membranes under a planar stress state. The sample is subjected to increased pressure until the failure happens. The specific point, where the failure ensues for the exposed membrane sample can be recorded as the bursting pressure or bursting strength [31]. The bursting strength of the samples was measured and plotted in Fig. 6. The strength of the neat N_0 was found to be 0.38 MPa, which was recorded lower than the tested composites. The analogous result was investigated by Yang et al. for the neat PSf membrane [32].

For C_1 nanocomposite, the upgraded strength of 0.45 MPa was accomplished. The probable explanation may be attributed to better interfacial interaction between PSf chains and $mSiO_2$. Several aspects, like smaller size of inserted filler, greater surface area, and higher stability might serve as a way to acquire exquisite blending at the interfacial region. Besides, the attachment of coupling agent conceivably assisted in the origination of a number of active centers, which reinforced the affinity and surface contact area between the two phases [33].

GO infused C_2 nanocomposite experienced curtailed burst strength of 0.42 MPa than the C_1 but a heightened value than the PSf membrane. The justification behind the lower strength might be due to the formation of aggregated morphology and restacking of layers. The π-π interaction might be the detrimental cause for shrinkage of GO dispersion within the matrix. As a consequence, it resulted in inferior polymer-filler interaction and a lessened strength was assigned to the membrane [30].

The hybrid membranes C_3 and C_4 have appraised greater burst strength of 0.69 and 0.61 MPa, respectively. The outstanding strength shall be explained on account of the synergistic effect between *in-situ* SiO_2 and nanosheets. The extreme manifestation of the existence of assorted functionalities on the surface of dispersed phase might have favored to accomplish excellent dispersive pattern [11]. The interspaces between the decorated SiO_2 and GO within the matrix acted as extensions to stimulate the adequate load transfer between the phases and enhanced the strength. However, the C_4

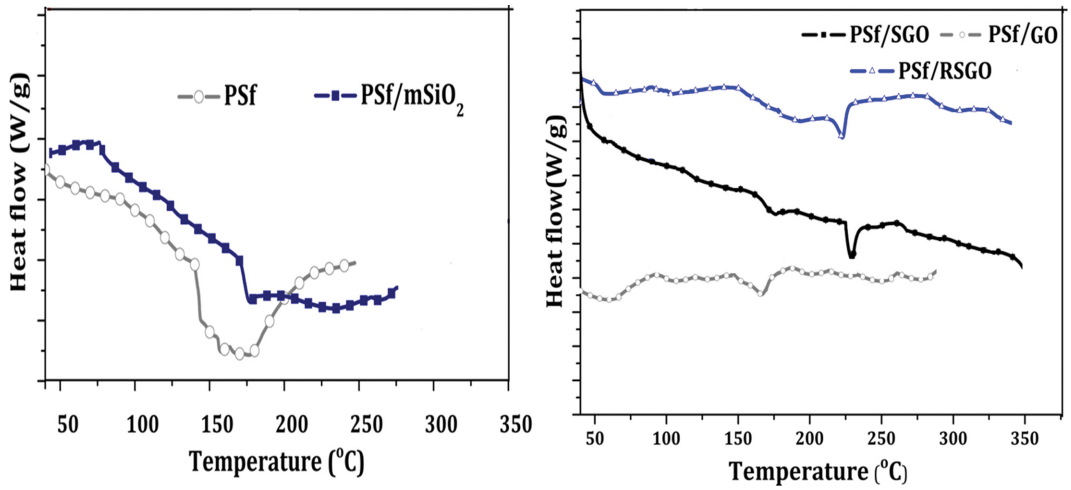

Fig. 7. DSC thermogram of pure PSf and investigated MMMs.

Table 1. T_g of investigated membrane systems

Sl. No.	Membrane samples	T_g (°C)
1	Neat PSf (N_0)	150
2	PSf/$mSiO_2$ (C_1)	175
3	PSf/GO (C_2)	170
4	PSf/SGO (C_3)	227
5	PSf/RSGO (C_4)	224

hybrid membrane displays a lessened value, which might be ascribed to the insertion of reduced graphene sheets with minimal oxidative groups. This dispersed phase possessed insufficient organo-functionalities and promoted devaluation in aspect ratio. Ultimately, RSGO revealed a slightly weaker membrane structure, in contrast to the SGO comprised system but still remained tenacious against the parent counterparts.

6. Thermal Properties (DSC and TGA)

6-1. Differential Scanning Calorimetry (DSC)

Fig. 7 shows the DSC thermograms of the neat and its composite membranes, while Table 1 outlines the attained T_g of the investigated samples. It was observed that the T_g increased in case of all the composites, irrespective of single or hybrid nature, which may be attributed to the reduced flexibility of the molecular chain segments.

N_0 membrane exhibited a wide range of T_g of 150 °C as described by Mannan et al. [34]. A perceptible increment in the T_g was registered for the single nanoscopic MMMs (PSf/$mSiO_2$ and PSf/GO). This behavior can be explained in terms of free volume concept; wherein the filler phases occupied the desired volume and increased the rigidity by virtue of the stress that arose during the fabrication of the nanocomposites structure. Consequently, higher thermal energy might be required for the rotation or consecutive movements of the chain segments within the developed MMMs [35].

C_1 system displayed an increased T_g of 175 °C. The interaction of small inorganic domains predominantly affected the long-range segmental mobility of the molecular chain segments. The organosilane moieties penetrated and entangled closely, which led to enhanced rigidity and restricted mobility of the matrix and caused to increase the T_g of PSf/$mSiO_2$ [33].

For C_2 membrane, a significant gain in the T_g value of 170 °C was registered. This can be explained owing to the bridge bonding between the PSf chains and GO containing rich-oxygen active functionalities [37]. The interaction between the carbon skeleton and oxygen moieties on the basal planes and edges boosted the affinity and assisted to revise the thermal stability of the neat membrane.

C_3 hybrid membrane displayed an enhanced T_g of 227 °C, which may be interpreted by the established synergistic effect between the *in-situ* decorated SiO_2 and oxidized graphene with the host matrix. Better exfoliation of the sheets enriched with silica led to maximum contact surface area and stimulated the dispersive characteristics by virtue of the colossal attachment of functional groups. Moreover, the covalently attached NPs are purported to act as solid-state exfoliating agents, which could have hindered the crumpling phenomena and facilitated a fine dispersion pattern within the entire volume of PSf [11]. The steric hindrance induced by the improved dispersion of the nanohybrid promoted the chain rigidification and heat flow rate [29]. Thus, a higher T_g was attained for the hybrid system.

For the RSGO based hybrid C_4 system, a T_g of 224 °C was recorded, which was ascribed to the penetration of transition zone surrounding the dispersed phase into the polymer chain gaps and vice-versa [30]. The absence of oxygen-rich functionalities led to a slight reduction in the T_g for the reduced hybrid system in comparison to SGO filled C_3 membrane.

6-2. Thermogravimetric Analysis (TGA)

TGA thermograms of the membranes are displayed in Fig. 8 and the related data are indexed in Table 2 in terms of initial degradation temperature (T_i), temperature at 10% (T_{10}) and 50% weight loss (T_{50}), final thermal degradation (T_d), and remaining % of char residue content. The thermograms depict three prominent stages of decomposition profile: corresponding to the desolvation of residual volatile moisture, thermal degradation of existing organic ligands, and disintegration of polymeric backbone as well as the carbonization of degraded products. The introductory weight loss was virtually initiated at a temperature above 100 °C, indicating the traces of

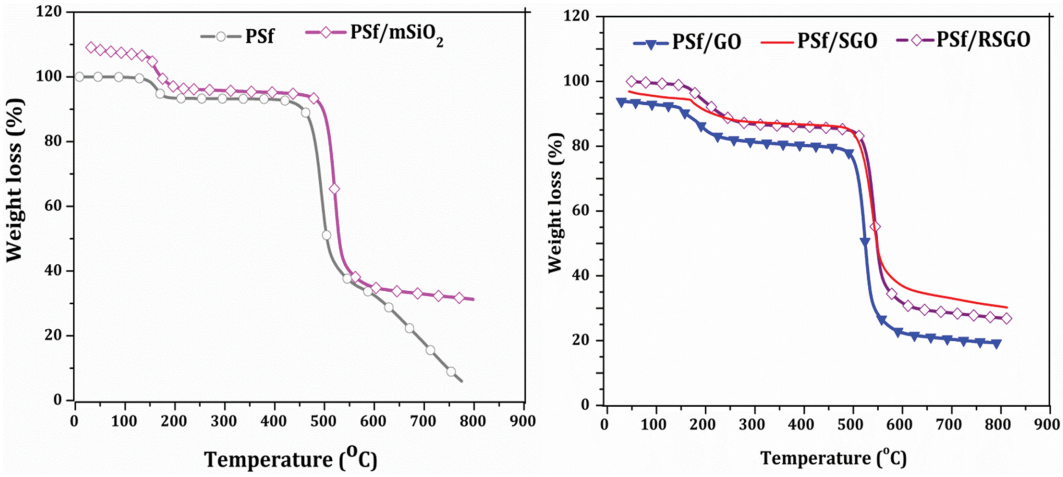

Fig. 8. TGA plots of the investigated membrane samples.

Table 2. TGA parameters of the investigated membranes

Sl. no	Samples	T_{on}	T_{10} (°C)	T_{50} (°C)	T_d (°C)	Char (%)
1	Neat PSf (N_0)	465	175	522	550	-
2	PSf/$mSiO_2$ (C_1)	476	183	524	568	27
3	PSf/GO (C_2)	472	198	525	555	26
4	PSf/SGO (C_3)	485	305	535	585	34
5	PSf/RSGO (C_4)	480	211	527	574	28

solvent or moistures over the surface of membranes.

The TGA plot of the neat sample demonstrated the primary loss was observed between 100° to 200 °C, signifying the removal of absorbed water molecule or excess solvent. The weight loss between 450-500 °C ensued owing to the degradation of polymer backbone and sulfone rupture. It displayed a complete degradation profile at 540 °C with no residue content [18].

C_1 membrane displayed an improved T_d at 568 °C. This might be assigned to rigidification of the chains at the interface owing to the close contact of $mSiO_2$ within PSf. As discussed in DSC, the SiO_2 particles caused restricted mobility of the chains and led to improved stability. High heat resistant silica particles could have trapped the volatile degradation and delayed the diffusion out of the polymer by virtue of the protection of pore-wall [17]. The pre-eminent mass loss within the range 450-520 °C was assigned to the degradation of the functionalities and decomposition of terminal absorbed amine groups [38]. The char residue of 27% along with improved T_{10} and T_{50} validated better stability of the C_1 system.

The inserted GO behaved like a mass transport barrier and limited the movement of the chain segments in C_2 [16]. The primary mass loss event under 250 °C shall be credited to the evaporation of residual moisture and presumable decomposition of polar group existed within the graphitic gallery. It accelerated the degradation, ultimately yielding CO, CO_2, and water as the by-products [18]. The eventual mass loss was credited to pyrolysis of the main backbone.

The thermogram of the C_4 hybrid system demonstrated the confined mobility of the segments at the interface and enhanced the stability with T_d of 585 °C. The intercalation of silica on the GO surface acted as bridge to facilitate the formation of an intimate link between the phases and reinforced the surface contact area [11]. The attachment of multi-functionalities behaved like a physical protective barrier, which could regulate the mobility of the chains and retard the degradation [39]. The char yield of 34% manifestly reflected the massive grafting of the functional groups on the surface of SGO inserted hybrid membrane. While for C_4 system, the mass loss of ~40% was assigned to the evacuation of remaining

Table 3. Permeability coefficients and selectivity of membrane systems

Sl. No.	Membrane samples	Permeability coefficients		Selectivity (α_{ij}) (O_2/N_2)
		O_2 (P_i)	N_2 (P_j)	
1	Neat PSf (N_0)	4.66	2.33	2
2	PSf/$mSiO_2$ (C_1)	9.41	4.08	2.30
3	PSf/GO (C_2)	7.79	3.75	2.07
4	PSf/SGO (C_3)	70.20	5	14.04
5	PSf/RSGO (C_4)	50.83	4.16	12.21

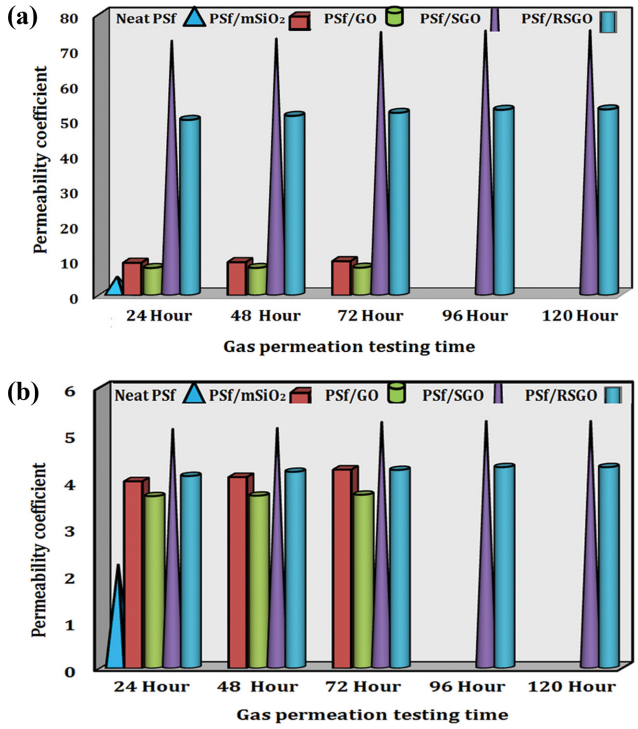

Fig. 9. (a) Long-term O_2 permeation stability of membrane systems, (b) Long-term N_2 permeation stability of membrane systems.

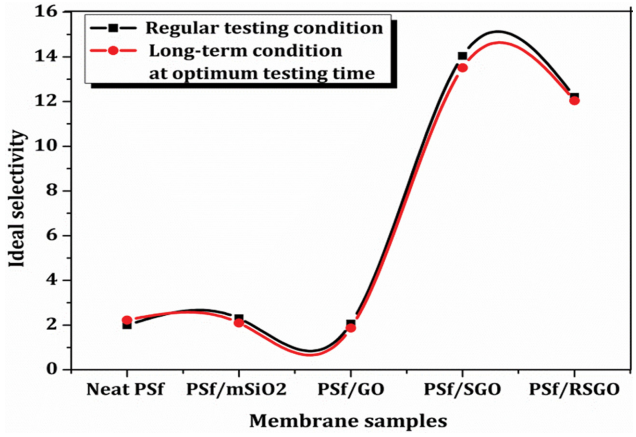

Fig. 10. Variation of selectivity of the systems at regular and long-term conditions.

residual groups and the subsequent burning of the graphitic sketch. Also, the tortuous path effect of graphene delayed the release of volatile degradation and improved the stability of the reduced hybrid system.

7. Stability Analysis

In our previous research [14], we measured the permeability coefficients of single gases (O_2 and N_2) through the neat PSf and its MMMs, including PSf/$mSiO_2$, PSf/GO, PSf/SGO, and PSf/RSGO. The permeability and ideal selectivity were analyzed and the recorded data compiled in Table 3. Here, we have studied long-term permeation testing, hydrothermal, and chemical stabilities of the membranes and inspected the discrepancy from the initially recorded values. These stability indexes can evaluate viability of the systems for large-scale gas separation and purification applications under realistic feed conditions.

7-1. Long-term Gas Permeation Stability

The long-term stability and durability factor of the samples were measured on account of the continuous permeation testing for a period of 120 hours without any obvious uninterrupted conditions. Fig. 9(a) and (b) illustrates the long-term stability of the membrane systems for penetrant gases O_2 and N_2, respectively, at each 24 hours of the permeation testing time, while Fig. 10 depicts the fluctuation in ideal selectivity at both regular and long-term conditions.

From Fig. 9, it was discerned that all the exposed membranes could not withstand 120 hours. Hence, permeation testing was continued till the sample was intact to convey the applied feed pressure or the measurement was terminated. From the plotted graphs, it can be revealed that the tested MMM systems maintained better long-term permeation stability than the neat PSf sample. After 24 hours of testing, the permeability of the native membrane for O_2 was marginally increased to 1.82% than the previously registered data; thereafter, the value was found constant at 4.89. Then measurement was automatically stopped. On removing the tested sample the ruptured surface with the emergence of cracks was identified. Meanwhile, the permeation rate of N_2 was recorded to be 2.20 at 36 hours. After this, the gas flow rate was stopped for the sample. From the graph, it can be affirmed that only a slight deviation in permeability and selectivity was documented for both the penetrant against the values as proclaimed at the routine testing conditions. Lower long-term permeation stability might be attributed to the decrement in free volume of the membrane skin layer or an increase in the thickness of the skin. The recorded curtailed burst strength with the mechanical deformation of the native PSf membrane than its nanocomposites further justified the above outcome.

But the tested MMMs displayed amplified steadiness contrary to the imposed conditions. C_1 and C_2 systems exhibited a perpetual permeation behavior till 72 hours and then the flow rate stopped and the measurement was disrupted. Both the penetrants showed a similar pattern as inspected antecedently in terms of smooth passage of O_2 and declined transportation for N_2.

The permeability coefficient of C_1 membrane for O_2 was 9.3, 9.48, and 9.75 at 24, 48, and 72 hours, respectively, while 7.8, 7.82, and 7.89 were recorded for the C_2 at the endorsed time period. N_2 permeabilities were noted at 4.25 and 3.71 after 72 hours of testing time for C_1 and C_2 systems, respectively. From the results, it was affirmed the permeability of the tested samples was improved even though marginally against the earlier data. Besides, the selectivity only slightly varied in opposition to the values as received at the regular parameters. The obligatory portrait for this cause of preeminent long-term permeation stability can be systematically shown taking into account the augmented burst strength against the native PSf as explained earlier. The enhanced stress transfer efficiency of C_1 and C_2 subsequently prompted sustainability to applied feed pressure for a longer period of time. The existence of fillers increased the affinity with the penetrants, which maximized

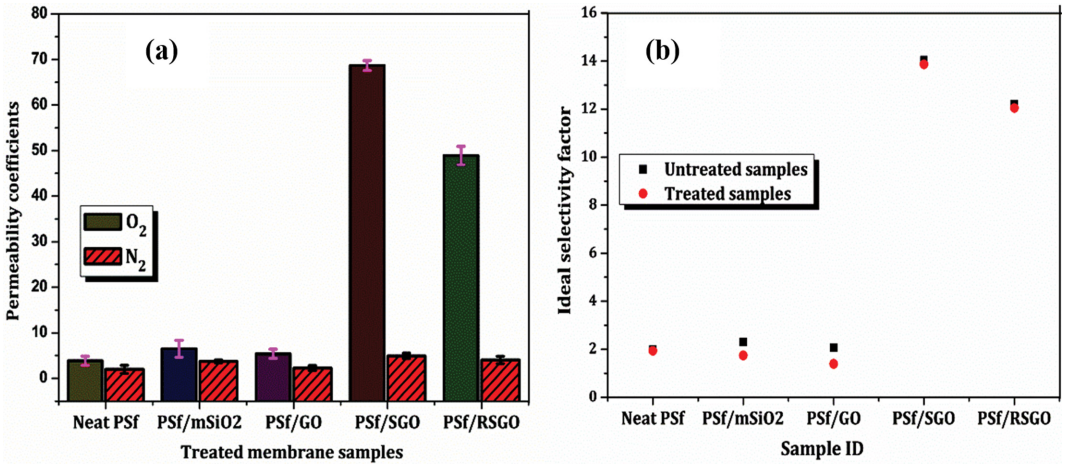

Fig. 11. Hydrothermal stability in terms of (a) permeability, (b) ideal selectivity.

the quota of interaction and improved the long-term stability. Further, the solubility and diffusivity of the penetrants might have increased with the appearance of the dispersed phase containing abundant functionalities on the surface. These facts might extend the testing time period [43].

The hybrid C_3 and C_4 systems showed improved permeability as well as selectivity as compared to their parent counterparts. These systems smoothly executed to finish the distinct period, which was resolved here to assess the long-term stability. It was observed the samples displayed splendid sustainability till 120 hours of testing time. No obvious damages, cracks, and holes were identified on the surface of the tested hybrid samples. During the long-term testing, it was noticed that within 24 hours the saturated permeation values were observed for the systems as recorded previously at the regular testing conditions.

The permeability of the C_3 sample was found to be 72, 72.66, 74.5, 74.89, and 75 while the C_4 hybrid system exhibited the values of 50, 51.15, 52.02, 52.89 and 53 at 24, 48, 72, 96, and 120 hours of testing time, respectively. For N_2 5.55 and 4.4 were measured at 120 hours. After completion of the prescribed time period, it was identified that the hybrid systems attained slightly higher permeability than the initial values. This increment might be attributed to the ensuing homogeneous interpenetrating architecture by virtue of enhanced surface area and the expanded volume of formulated deformation zone with the insertion of hybridized sheets into the host matrix. Besides, the existence of a number of nanochannels, intersegmental spacing, along with the conspicuous emanation of auxiliary cavities or polar sites assisted the findings of ameliorated long-term stability of the hybrid membranes [3]. These circumstances possibly enlarged the stability so that the exposed samples emphatically conveyed the enforced feed pressure for a longer time period without any deterioration in structure and performance. This might be the relevant cause for the improved long-term stability of the hybrid systems.

Additionally, the augmented burst strength of the hybrid samples than their counterparts has supported the findings. The attachment of multifunctionalities on the hybridized sheets might stimulate to maintain the stability and steady permeability for longer time. It was divulged the hybrid systems displayed excellent stability and durability even after long-term exposure.

7-2. Hydrothermal Stability

The tolerance of water vapor treated samples towards the permeation analysis was observed. Fig. 11(a) represents hydrothermal stability of the treated systems, meanwhile (b) shows the selectivity of the treated and untreated samples.

From the plotted graphs, it can be demonstrated that the permeability characteristics of the treated C_1 and C_2 nanocomposites were predominantly affected. Meanwhile, the neat PSf and hybrid systems only marginally varied even after exposure to the controlled water vapor environment. In our previous report [14], we discussed the hydrophilization behavior of the membranes in terms of water contact angle (WCA) measurement. From the analysis, it was observed that the single filler based systems rendered hydrophilic nature, but a preponderant shift towards hydrophobicity was recognized for the PSf and tested hybrid samples. Thus, it is apparent that the permeation demeanor of the hydrophilic membranes would be distressed more by the vapor treatment than the hydrophobic one. Depending on the surface nature from WCA, the influence of the treatment on the gas permeation characteristics can be expected in order of PSf/GO>PSf/$mSiO_2$>PSf>PSf/SGO>PSf/RSGO. This treatment established a weak influence on the permeation behavior of the treated C_1 and C_2 with reduced values for O_2 in the order of 6.25 and 4, while 4 and 2.25 were noted for N_2. However, the treated N_0 and hybrid samples were only marginally affected. 4.08 and 2.15 were registered for O_2 and N_2, respectively, for the treated N_0. C_3 showed permeability of 61.51 and 4.05 after the treatment, but the treated C_4 only slightly varied with moderate selectivity. The declining performance can be explained owing to the ensued plasticization effect of absorbed moisture on the surface of treated samples. The adhered vapor may indicate the formulation of intra-sheet hydrogen bonding between the existing functionalities of different fragments. It might have facilitated the origination of bridge network on the hydrophilic samples. This phenomenon precluded the smooth openings of transport avenues, free gaps, and channels, which prevented the resistance-free permeation. It can be declared that the performance predominantly

Table 4. Outlines chemical stability in terms of selectivity of membrane systems

Sl. No.	Membrane samples	Selectivity ($\alpha_{i/j}$) (O_2/N_2)		
		Untreated	Treated samples in acidic medium	Treated samples in alkaline medium
1	Neat PSf	2	2.12	2.05
2	PSf/$mSiO_2$	2.30	2.36	2.23
3	PSf/GO	2.07	2.01	2.19
4	PSf/SGO	14.04	14	14.02
5	PSf/RSGO	12.26	12.24	12.26

relies upon the intensity of oxygen-rich or hydrophilic groups on the sample surface. It can be concluded that the specimen containing polar moieties would display lower hydrothermal stability and reduced permeation characteristics under moist conditions.

7-3. Chemical Stability

After the chemical treatment in both acidic and alkaline media, the treated samples were exposed to analyze the permeation characteristics for the targeted penetrants. Table 4 outlines the selectivity of untreated and chemically treated samples. The permeability of the treated N_0, C_1, and C_2 was only marginally varied against the untreated ones; meanwhile, the hybrid systems displayed almost similar values as the original. Irrespective of the type of nanofiller (single or hybrid), the samples displayed excellent chemical stability. This may be ascribed to the inherent chemical inertness of the PSf backbone. It can be conceded these systems are stable under acidic and alkaline media, justifying their suitability for intended applications.

CONCLUSIONS

We prepared high performance PSf based MMM systems. The membranes were prepared by taking nanofillers inclusive of $mSiO_2$, GO, SGO and RSGO. XRD, Raman, and UV spectroscopy were done to affirm the existence of inserted fillers within the matrix. TEM imaging was performed to acquire knowledge on dispersive characteristics. The thermal properties (DSC and TGA) were investigated; the hybrid system displayed improved thermal stability among all the tested samples. Silica decorated graphene based hybrid system showed improved performance in terms of excellent permeability and selectivity as compared to the parent and native membranes. The hybrid systems retained numerous channels, free spaces, and active sites for smooth permeation of gases over the counterparts. Thus, the systems proved themselves as qualified candidates for large-scale gas separation applications. The hydrothermal and chemical stability over the permeation characteristics of the samples supported the derived conclusion on the pertinence of the hybrid MMM systems for a range of commercialization in the separation field.

ACKNOWLEDGEMENTS

The authors would like to thank Science and Engineering Research Board (SERB), Department of Science & Technology (DST), New Delhi for financial assistance for the project. Also, the authors declare that they have no conflict of interest.

NOMENCLATURE

MMMs : mixed matrix membranes
NPs : inorganic nanoparticles
GO : oxidized graphene
$mSiO_2$: APTES modified nano silica
SGO : silica decorated oxidized graphene
RSGO : silica decorated reduced graphene
P : permeability coefficient
P_i/P_j : permeability coefficient of gas (i) over (j)
$\alpha_{i/j}$: selectivity factor
l : thickness of membrane sample

SUPPORTING INFORMATION

Additional information as noted in the text. This information is available via the Internet at http://www.springer.com/chemistry/journal/11814.

REFERENCES

1. S. S. Swain, L. Unnikrishnan, S. Mohanty and S. K. Nayak, *Inter. J. Hydro. Ener.*, **42**, 29283 (2017).
2. G. Dong, H. Li and V. Chen, *J. Mater. Chem. A*, **1**, 4610 (2013).
3. S. S. Swain, L. Unnikrishnan, S. Mohanty and S. K. Nayak, *J. Mat. Sci.*, **53**, 15442 (2018).
4. S. Ishaq, R. Tamime, M. R. Bilad and A. L. Khan, *Sep. Purif. Tech.*, **210**, 442 (2018).
5. H. Wu, B. Tang and P. Wu, *J. Membr. Sci.*, **451**, 94 (2014).
6. L. C. Fonseca, A. C. Moraes, D. Silva, A. G. Ferreira, L. S. Franqui, D. T. Martinez and O. L. Alves, *Appl. Surf. Sci.*, **437**, 110 (2018).
7. Z. K. Li, W. Z. Lang, W. Miao, X. Yan and Y. J. Guo, *J. Membr. Sci.*, **511**, 151 (2016).
8. Y. Maa, H. Di, Z. Yu, L. Liang, Y. Pan, Y. Zhang and D. Yin, *Appl. Surf. Sci.*, **360**, 936 (2016).
9. M. S. Wang, Z. Q. Wang and Y. Yang, *Appl. Sur. Sci.*, **456**, 379 (2018).
10. S. A. Jin, S. Poudyal, E. E. Marinero, R. J. Kuhn and L. A. Stanciu, *Electrochim. Acta*, **194**, 422 (2016).
11. S. Z. Haeri, B. Ramezanzadeh and M. Asghari, *J. Collo. Interf. Sci.*, **493**, 111 (2017).
12. D. Rana, H. L. Kim, C. Rhee, T. Woo, S. H. Park and S. Choe, *Annual Technical Conference - ANTEC*, **45**(3), 3775 (1999).
13. S. S. Swain, L. Unnikrishnan, S. Mohanty and S. K. Nayak, *Appl. Nanoscience*, **9**, 1 (2019).
14. S. S. Swain, L. Unnikrishnan, S. Mohanty and S. K. Nayak, *Poly-*

mer, **180**, 121692 (2019).
15. Y. Ma, F. Shi, Z. Wang, M. Wu, J. Ma and C. Gao, *Desalination*, **286**, 131 (2012).
16. M. Ionita, A. M. Pandele, L. E. Crica and A. C. Obreja, *High Performance Polymers*, **28**, 181 (2015).
17. S. Rafiq, Z. Mana, A. Maulud, N. Muhammada and S. Maitra, *Sep. Purif. Tech.*, **90**, 162 (2012).
18. M. Ionita, A. M. Pandele, L. Crica and L. Pilan, *Com: Part B*, **59**, 133 (2014).
19. Z. Liu and Y. Zhang, *Comp: Part A.*, **102**, 236 (2017).
20. S. Z. Haeri, M. Asghari and B. Ramezanzadeh, *Prog. Org. Coat.*, **111**, 1 (2017).
21. T. Adachi, M. Osaki and W. Araki, *Acta Materialia*, **56**, 2101 (2008).
22. S. Prasertsri, F. Lagarde, N. Rattanasom, C. Sirisinha and P. Daniel, *Poly. Testing*, **32**, 852 (2013).
23. J. Lee, H. Chae, Y. Won, K. Lee, C. H. Lee and I. Kim, *J. Membr. Sci.*, **448**, 223 (2013).
24. Z. Liu, H. Zhang and Y. Zhang, *Com. Sci. Technol.*, **150**, 174 (2017).
25. M. S. Jyothi, V. Nayak, M. Padaki, R. G. Balakrishna and A. F. Ismail, *Desalination*, **354**, 189 (2014).
26. I. Dueramae, C. Jubsilp and T. Takeichi, *Com. Part: B*, **56**, 197 (2014).
27. M. Parvinzadeh, *Appl. Surf. Sci.*, **256**, 2792 (2010).
28. M. J. Park, S. Phuntsho, T. He, G. M. Nisola, L. D. Tijing, X. M. Li, G. Chen, W. J. Chung and H. K. Shon, *J. Membr. Sci.*, **493**, 496 (2015).
29. S. Pourhashema, M. R. Vaezi and A. Rashidi, *Surf. Coatings Technol.*, **311**, 282 (2017).
30. P. G. Su, *Talanta*, **132**, 398 (2015).
31. K. Wang, A. A. Abdalla, M. A. Khaleel, N. Hilal and M. K. Khraisheh, *Desalination*, **401**, 190(2017).
32. Y. Yang, P. Wang and Q. Zheng, *J. Poly. Sci: Part B: Poly. Phy.*, **44**, 879 (2006).
33. H. Gu, Y. Guo, S. Y. Wong, X. Li and V. P. W. Shim, *Compo. Sci. Technol.*, **75**, 62 (2013).
34. H. A. Mannan, H. Mukhtar, M. S. Shaharun, M. R. Othman and T. Murugesan, *J. Appl. Polym. Sci.*, **42946**, 1 (2016).
35. H. Wu, X. Li, S. Wang, Z. Jiang, Q. Xin and X. Lu, *J. Membr. Sci.*, **465**, 78 (2014).
36. M. Bhattacharya, *J. Cleaner Prod.*, **186**, 241 (2018).
37. L. Dong, M. Chen and X. Li, *J. Membr. Sci.*, **520**, 801 (2016).
38. M. F. Wahab, A. F. Ismail and S. J. Shilton, *Sep. Purif. Technol.*, **86**, 41 (2012).
39. G. Wu, L. Ma, L. Liu, L. Chen and Y. Huang, *Thermochim. Acta*, **613**, 77 (2015).
40. R. Jeziórska, B. Gutarowska and Z. Zakowska, *Inter. J. Polym. Sci.*, **10**, 1 (2014).
41. M. Ionita, L. E. Crica, E. Vasile, M. A. Pandele and J. Haugen, *Polymer*, **92**, 1 (2016).
42. C. Monteserín, M. Blanco, E. Aranzabe, A. Aranzabe, J. M. Laza, A. L. Varga and J. L. Vilas, *Polymer*, **9**, 449 (2017).
43. S. S. Swain, L. Unnikrishnan, S. Mohanty and S. K. Nayak, *Korean. J. Chem. Eng.*, **34**, 2119 (2017).

Supporting Information

Insight into mechanical, thermal, and chemical stability of polysulfone-based membranes for the separation of O_2/N_2

Suchhanda Srabanee Swain†, Lakshmi Unnikrishnan, Smita Mohanty, and Sanjay Kumar Nayak

School for Advanced Research in Polymers (SARP), Laboratory for Advanced Research in Polymeric Materials (LARPM),
Central Institute of Plastics Engineering & Technology (CIPET), B/25, CNI Complex,
Patia, Bhubaneswar - 751024, Odisha, India
(*Received 18 March 2021 • Revised 27 July 2021 • Accepted 15 August 2021*)

1. XPS Analysis of SGO and RSGO

The signals of O1s, N1s, C1s, Si2s, and Si2p were discerned in the SGO spectrum as shown in Fig. S1(a). The C1s spectrum can be deconvoluted into five Gaussian-Lorentzian peaks related to C=C (284.2 eV), C-Si (283.7 eV), C-O-Si (285.9 eV), C-N (286.3 eV), and C-O (287.7 eV). It confirmed the precipitation of *in-situ* silane moieties on the surface of oxidized nanosheets with the formation of strong covalent linkage. Additionally, the Si2p spectra were fitted by two peaks assigned to Si-C and Si-O-Si bonds with binding energies of 101.4 eV and 102.8 eV, respectively. The O1s signal can be separated into five Gaussian-Lorentzian peaks, including O-C=O (530.1 eV), C=O (531.3 eV), C-O-Si (532.2 eV), Si-O-Si (532.8 eV), and C-O-C/OH (533.9 eV). The disappearance of C-O-C peak of epoxide groups and the emergence of a new C-N peak at 286.4 eV validated the reaction between GO and APTES molecules. From the results, it can be revealed that APTES and TEOS mostly grafted in the form of SiO_2 particles on the surface of GO. These observations are completely in accordance with the results as reported in literature [1-3].

In the RSGO spectrum, as shown in Fig. S1(b) the peak intensity of O1s signals assigned to oxygen-rich functionalities were decreased relative to SGO. In C1s signal, the major sp^3 carbon dominated band at 284.5 eV was observed. The common peak over the range of 290-294 eV appeared in the spectra, which might be assigned to delocalized π-π conjugation. This occurrence confirmed the trend of restoration of sp^2 network of graphene sheets. It is a consistent signature of extreme deoxygenation of SGO [4]. Additionally, a noteworthy fact was noticed; the extent of NPs coverage was found unaffected after the reduction process. The appearance of the peaks related to Si2s and Si2p confirmed the attachment of SiO_2 on the surface. The small content of the residual oxygen groups may be ascribed to the existence of -COOH in the decomposition product. This fact might be elucidated on the basis of the incomplete neutralization of the reductant. However, it can be observed that the intensity of the peaks related to oxygen-carrying groups greatly reduced in the case of RSGO than the SGO nanohybrid. The detailed discussions have been represented in our previous report entitled "Synthesis andcharacterization ofsurface-functionalized mesoporous graphene nanohybrid, Appl. Nano. (2019) 1-22. https://doi.org/10.1007/s13204-019-00963-0 1-22**.**

2. Gas Permeation Analysis of Hybrid Systems

The hybrid systems (PSf/SGO and PSf/RSGO) were found to have improved permeabilities against the unfilled or single filler blended parent nanocomposite membranes (PSf/mSiO_2 and PSf/GO). The permeability coefficients for PSf/SGO were observed to be 70.20 and 8 for O_2 and N_2 respectively. The hybrid system depicted 645% and 801% higher O_2 permeabilities than the PSf/mSiO_2 and PSf/GO, respectively. The higher permeability might be attributed to the surface decoration of GO with *in-situ* silane moieties, which resulted in weakened π-π interaction, favoured uniform and homogeneous distribution of the nanohybrids throughout the entire volume of the host matrix [2]. The unique structure of these nanohybrids might have reduced the chances of aggregation and prompted an intimate interaction with the PSf. Thus, the insertion of these hybridized fillers may increase the surface contact area and positively alter the interfaces to perform better than their parent counterparts. Wu et al. [5] recorded water purification performance of SiO_2-GO inserted MMM system. However, to the best of our knowledge, these hybridized fillers have not been utilized to prepare the MMMs for studying any gas permeation analysis.

The uniform intercalation and improved surface area of these nanohybrids might be provided the suitable avenue for the formulation of a number of channels. And these channels could promote the origination of excessive free volume gaps, polar sites, and a number of selective cavities at the polymer-hybridized fillers interface by virtue of the localized disturbances. As a consequence, the penetrants could easily transport through these nanogaps existed at the inter-segmental spacing and on the surface of hybridized fillers. These facts intensified the permeabilities of the hybrid systems than the corresponding parent membranes. Further, the synergistic influence contributed to improving the selectivities of O_2/N_2 for the SGO hybrid membrane in the order of 14, which exceeded the well-known Robeson upper bound trade-off limit (2008) [6]. Meanwhile, the permeabilities of PSf/RSGO were found to be 50.83 and 4.46 for O_2 and N_2, respectively. The higher permeabilities can be interpreted as follows: the hybridized reduced nanosheets contain contiguous hydrophobic aromatic surface and the remaining functionalities might act as spacers to prevent the formation of an overtight laminate structure within the PSf matrix. Additionally, the reduced dispersed phase might be behaved as the molecular sieving framework and effectively hindered the transport of N_2 by creating a long and tortuous path [7]. A complete description of the permeation analysis of gaseous species through the hybrid and single filler blended nanocomposites has been investigated in our ear-

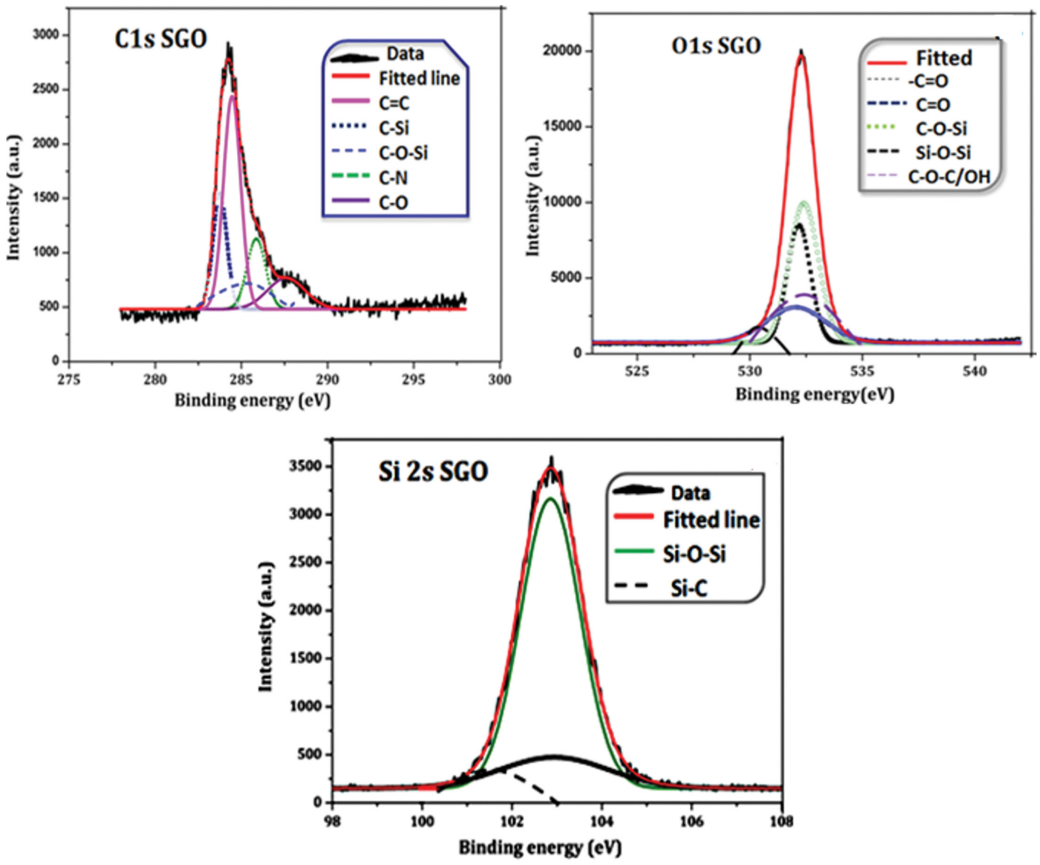

(a)

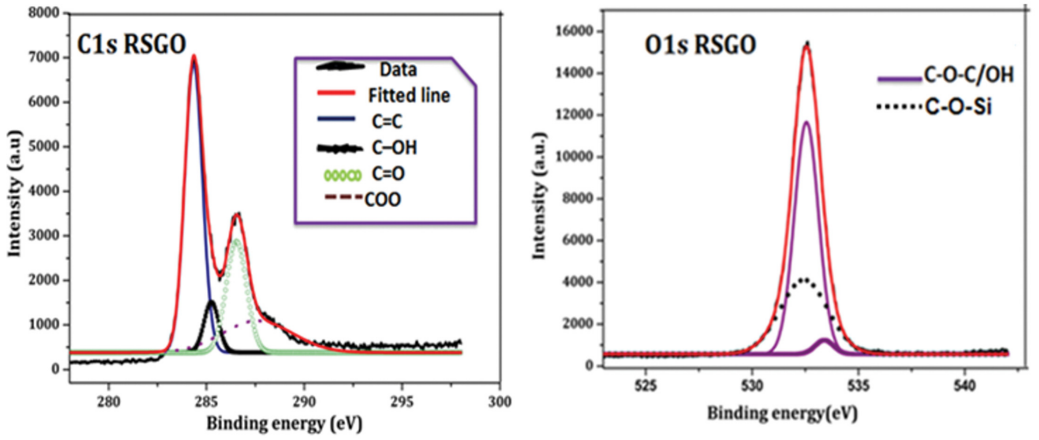

(b)

Fig. S1. (a) XPS analysis of SGO, (b) XPS analysis of RSGO.

lier paper entitled "Gas Permeation and Selectivity Characteristics of PSf based Nanocomposite Membranes" POLYMER 180 (2019) 121692. https://doi.org/10.1016/j.polymer.2019.121692.

REFERENCES

1. S. Z. Haeri, B. Ramezanzadeh and M. Asghari, *J. Col. Interf. Sci.*, **493**, 111 (2017).
2. B. Ramezanzadeh, H. Haeri and M. Ramezanzadeh, *Chem. Eng. J.*, **303**, 511 (2016).
3. W. L. Zhang and H. J. Choi, *Langmuir*, **28**, 7055 (2012).
4. X. Pu, H. B. Zhang, X. Li, C. Guia and Z. Zhen, *RSC Adv.*, **4**, 15297 (2014).
5. H. Wu, B. Tang and P. Wu, *J. Memb. Sci.*, **451**, 94 (2014).
6. K. C. Chong, S. O. Lai, H. S. Thiam, H. C. Teoh and S. L. Heng, *J. Eng. Sci. Technol.*, **11**, 1016 (2016).
7. S. A. Mohammed, A. M. Nasir, F. Aziz, G. Kumar, W. Sallehhudin, J. Jaafar, W. J. Lau, N. Yusof, W. N. Salleh and A. F. Ismail, *Sep. Purif. Tech.*, **223**, 142 (2019).